RSC Mechanochemistry

ROYAL SOCIETY OF CHEMISTRY

PAPER

View Article Online
View Journal | View Issue

Cite this: *RSC Mechanochem.*, 2025, **2**, 923

Exploring milling atmosphere effects in mechanochemical synthesis of Pd–Cu supported catalysts for the semihydrogenation of acetylene in equimolar ethylene mixtures

Rohini Khobragade, † Jonathan M. Mauß, † Nguyen Khang Tran and Ferdi Schüth*

Supported bimetallic nanoparticles (NPs) have evolved as promising candidates for heterogeneous catalysis. Among various synthesis methods, ball milling has recently emerged as an effective approach for the preparation of high performing catalysts in diverse applications. Recognizing that solid–gas interactions in such a solvent-free environment might be crucial, we investigated the influence of the gas atmosphere (oxidative, inert, and reductive) during ball milling on the structural and electronic properties of Pd–Cu alloy NPs supported on high surface area α-Al_2O_3. Milling under an oxidative atmosphere leads to Cu-segregation to the surface, forming CuO, PdO, and a small fraction of metallic Pd alongside the Pd–Cu alloy phase. In contrast, in the case of an inert atmosphere, the major phase is the Pd–Cu alloy with a very minimal fraction of unalloyed metallic components. Milling under a reductive atmosphere reveals reverse segregation with metallic Pd segregating to the surface. Additional thermal treatment further promotes the alloy formation in all cases, but oxide species from synthesis under oxidative atmosphere are retained. Unveiling structure–property correlations, the materials were tested in the catalytic selective hydrogenation of acetylene to ethylene in equimolar acetylene/ethylene mixtures under industrially relevant pressure. Results demonstrate that the ball-milling atmosphere significantly influences catalytic performance, driven by the structural and electronic variations induced during synthesis. This study underscores the critical role gas environments may have in mechanochemical processes and highlights their potential to fine-tune catalyst properties for improved performance.

Received 5th June 2025
Accepted 9th September 2025

DOI: 10.1039/d5mr00074b

rsc.li/RSCMechanochem

Introduction

Supported bimetallic catalysts gained significant recognition in various established and emerging industrial and environmental applications, owing to their enhanced catalytic activity, tunable selectivity, long-term stability, and cost-effectiveness.[1–3] The dynamic nature of supported bimetallic catalysts is influenced by the surrounding atmosphere, which can induce surface reconstruction through oxidation, reduction, and segregation processes. These changes alter the catalyst's electronic and geometric structures. Consequently, significant progress has been made in understanding how different gas atmospheres can alter the electronic and chemical structures of supported bimetallic catalysts.[4–6]

Several reports comprising both theoretical[7–10] and experimental[7,11–14] studies highlight the significant impact of gas atmospheres on the structural evolution of alloy NPs. For instance, Huang *et al.* demonstrated that Pt–Cu alloy NPs supported on TiO_2 undergo de-alloying upon oxidation, which leads to the dispersion of CuO on the support surface. However, subsequent reduction results in partial re-alloying of surface Cu with Pt, significantly altering the surface structure.[15] Further, Kalyva *et al.* investigated Pt–Cu and Pt-supported catalysts under oxidative and reductive cycles at elevated temperatures, resulting in changes of size and composition due to the leaching of Cu at higher temperatures.[16] However, those and many other reports on surface segregation phenomena in alloy NPs during heat treatment under different gas atmospheres or vacuum so far focus exclusively on conventionally synthesized materials.[7,13,17,18]

Mechanochemical synthesis, primarily through high-energy ball milling, has evolved as a scalable, cost-effective, solvent-free, and environmentally friendly alternative synthesis pathway and gained attention for industrial applications.[19,20] Our group developed a mechanochemical synthesis method for supported monometallic NPs, which has recently been extended to bimetallic systems. Milling bulk metal precursors

Department of Heterogeneous Catalysis, Max-Planck-Institut für Kohlenforschung, Kaiser-Wilhelm-Platz 1, 45470 Mülheim an der Ruhr, Germany. E-mail: schueth@kofo.mpg.de

† Rohini Khobragade and Jonathan M. Mauß contributed equally to this work.

and support together in a high-energy regime yielded supported alloy NPs in an easy one-step procedure.[21,22] This approach proved to be effective for the synthesis of various alloy NPs on different support materials, for instance, Au–Cu, Au–Pd, Ag–Pd, or Pd–Pt on MgO, yttrium-stabilized ZrO_2 or high surface area α-Al_2O_3. For various reactions the resulting materials typically have catalytic performance similar to catalysts synthesized *via* traditional, more complex pathways.[22–24] Our group also proposed a plausible model to understand the mechanism of mechanochemical synthesis of supported bimetallic catalysts by providing a better control of particle dispersion and alloying based on metal-support oxide interaction.[24] Many different parameters such as milling frequency, ball size, milling time, and precursor addition sequence have been explored to understand the relevant factors in tailoring the properties of the resulting materials.[25–29] Recently, a study demonstrated the importance of milling atmosphere for CO oxidation using a monometallic palladium catalyst supported on cerium oxide, highlighting the influence of oxidative, inert, and reductive atmospheres on catalytic activity.[30] However, although the gas atmosphere during milling might be expected to have a substantial influence, to the best of our knowledge, there is so far no systematic study in this direction for supported bimetallic catalysts.

Herein, we explore the influence of different gas atmospheres during ball milling synthesis of Pd–Cu alloy NPs supported on α-Al_2O_3. We intentionally selected the Pd–Cu bimetallic composition due to the full solubility range of Pd and Cu, which has been extensively studied for their segregation behaviour under various gas atmospheres for conventional synthesis methods.[6,18,31–33] Additionally, α-Al_2O_3 was selected as the support due to its high surface area and stability after mechanochemical synthesis, making it highly relevant for industrial applications.[34–38] To explore structure–property correlations, especially with regard to potential applications of the materials, we also investigated catalytic properties in the selective hydrogenation of acetylene in equimolar acetylene–ethylene mixtures, which would result from a hypothetical plasma-based methane-to-ethylene conversion plant.[23,39] These conditions are unusual and highly challenging, since in conventional selective acetylene hydrogenation only small partial pressures of acetylene are present, so that the high exothermicity and explosion risks are less of a problem. Due to the harsh requirements on catalysts to exhibit selective behaviour at such high acetylene concentrations and difficult temperature control, these reaction conditions represent an ideal tool to assess the quality of alloy formation in bimetallic materials. By coupling analytical results with catalytic behaviour, this study aims at understanding how the gas environment during a mechanochemical synthesis affects alloy formation of palladium and copper and allows to tailor surface chemistry.

Experimental

Materials and methods

Materials. Boehmite (γ-AlOOH, Sasol, DISPAL 11 N7-80, Lot No. S4486J, specific surface area (S_{BET}): 67.3 $m^2\ g^{-1}$), palladium powder (Pd, Alfa Aesar, −200 mesh, 99.95% metal basis), copper powder (Cu, Alfa Aesar, −170/+400 mesh, >99.9% metal basis), palladium(II) nitrate dihydrate ($Pd(NO_3)_2 \cdot 2H_2O$, Sigma Aldrich, ~40% Pd basis), copper(II) nitrate trihydrate ($Cu(NO_3)_2 \cdot 3H_2O$, Merck, >99.5%), quartz wool (Roth, chemically pure), silicon carbide (Alfa Aesar, 46 grit). All the reagents were used without any further purification.

General ball milling equipment. Fritsch Pulverisette 7 planetary ball mill (P7, classic line) was used with two 45 ml zirconia jars and three 15 mm diameter zirconia balls for each jar, maintaining a ball-to-powder ratio of 33 : 1.

Mechanochemical synthesis of supported Pd–Cu catalyst in different atmospheres

Oxidative (air) atmosphere. All the steps throughout the synthesis were performed in an air atmosphere. Firstly, the jars were charged with the bulk metal powder precursor of unity molar ratio of Pd and Cu targeting 5 wt% (Pd + Cu 50 mg) and milled for 30 min at 550 rpm. Using bulk metal powders eliminates solvent-based steps and purification, making the synthesis more sustainable. Further, the same jars were charged with γ-AlOOH (950 mg), a precursor for α-Al_2O_3, and milled at 500 rpm for 6 h. To ensure not to overheat the jars, the milling has been performed in cycles of 15 min milling followed by a 5 min break. Finally, the synthesized material was recovered by scratching it out from the jar and balls.

Inert (argon) atmosphere. To make a fair comparison, all the synthesis steps are the same as those of the oxidative atmosphere. The steps, including loading the precursors into jars and collecting samples after ball-milling synthesis, were performed inside the glove box to ensure an inert atmosphere (Ar) throughout the synthesis.

Reductive (H_2) atmosphere. Our in-house design and manufactured high-pressure P6 milling jar[40] with a stainless steel outer and zirconia inner jar (45 ml) overcame the limitations of the P7 milling jar where it was difficult to maintain the reductive milling atmosphere. Fig. S1 shows the picture of the outer stainless steel jacket and inner ZrO_2 jar (45 ml). However, due to the inside design of the jar, ten 10 mm ZrO_2 balls were required to achieve the same catalytic phase as in the P7 milling jar. After loading the precursor, the jar was carefully sealed using a 20 Nm torque wrench. Before filling the H_2 gas, first, the jars were evacuated and the step of injection of Ar gas and evacuation was repeated three times to ensure an oxygen-free atmosphere. Finally, H_2 gas was pressurized (5–6 bar) and the milling steps were carried out in the same way as for the oxidative and inert atmospheres.

Thermal treatment. Regardless of the synthesis method, all the catalysts were subjected to thermal treatment in hydrogen atmosphere. The materials were first treated at 150 °C for 3 h and then at 600 °C for 2 h in pure H_2 flow (flow rate 100 ml min^{-1}). Subsequently, the samples were subjected to an additional annealing step at 600 °C for 8 hours under an argon flow (flow rate 100 ml min^{-1}).

For all three oxidative, inert, and reductive atmospheres, a series of supported Pd_xCu_y catalysts was also synthesized with the ratio $x : y$; 1 : 0, 1 : 5; 1 : 9; 0 : 1.

Characterization methods. Powder X-ray diffraction (p-XRD) measurements were performed using a Rigaku SmartLab X-ray diffractometer equipped with a 9 kW rotating anode, operating at 45 kV and 200 mA in Bragg–Brentano-geometry (Cu $K\alpha_{1,2}$ λ: 1.541862 Å). The data were collected continuously in the 10–70° 2θ range with angular step size 0.01° and scan speed 0.5° min^{-1}, by using HyPix-3000 multi-dimensional detector in 1 D mode. XRD data analysis was carried out by using the ICCD PDF-2 pattern database. The N_2 physisorption measurements of the catalysts were performed on a 3Flex Micromeritics instrument at 77 K. All the samples were degassed under vacuum at 350 °C for 1 h prior to the measurement. The Brunauer–Emmett–Teller (BET) method was used to calculate the specific surface area from the data in the relative pressure range of 0.05 to 0.3. The size and morphology of the catalysts were analyzed by high angle annular dark-field scanning transmission electron microscopy (HAADF-STEM) with a Hitachi HD 2700 microscope operating at an accelerating voltage of 200 kV attached with cold field-emission cathode gun and EDAX Octane T ultra W 200 mm^2 SDD. The energy dispersive X-ray spectroscopy (EDXS) elemental maps and high-resolution transmission electron (HR-TEM) images were acquired using the same microscope. The samples were prepared by carefully sprinkling them onto a lacey carbon grid, which in turn was supported by a copper grid. The particle size distribution was determined by measuring more than 200 particles across at least 10 different images. The elemental composition of the catalysts was determined by energy dispersive X-ray (EDXS) bulk analysis by using Hitachi TM3030 Plus table-top scanning electron microscopy. The microscope was equipped with an Oxford Instruments GmbH Si(Li) Pentafet Plus detector, and the acceleration voltage was set to 25 kV. Additionally, all samples used for scanning electron microscopy (SEM) measurements were prepared by gently sprinkling the dry specimens onto a C-film. Inductively coupled plasma optical emission spectroscopy (ICP-OES) measurements were carried out on the SPECTRO-GREEN instrument to determine the chemical composition and metal loading of the catalysts. The samples were digested in aqua-regia ($HCl : HNO_3$, 3 : 1 v/v) overnight followed by dilution using Ultra-pure Milli-Q water (18.2 MΩ cm). Further, the samples were filtered by using the PTFE filter to remove any remaining solids before measurements. X-ray photoelectron spectroscopy (XPS) measurements were performed on SPECS GmbH spectrometer equipped with hemispherical analyser (PHOIBOS 150) and 1 D-DLD detector. The monochromatized Al Kα X-ray source (E = 1486.6 eV) was operated at 15 kV and 200 W. The survey scan was measured with an acceleration energy of 50 eV, while a pass energy of 20 eV was applied for the narrow scan. For the lens mode, the medium area mode was used. A 5×10^{-10} mbar base vacuum was maintained during the experiment. The C 1s peak with binding energy 284.5 eV was used to correct for surface charging (Fig. S5). H_2-temperature programmed reduction (H_2-TPR) analysis was carried out on AutoChem Micromeritics 2920 instrument equipped with a thermal conductivity detector (TCD). About 110 mg to 120 mg of the sample was loaded in a U-shaped quartz reactor. The sample was first pre-treated in a flow of Ar (50 ml min^{-1}) at 200 °C for 1 h and cooled down to room temperature. The analysis was carried out in a flow of 10% H_2/Ar (50 ml min^{-1}) by heating the sample from room temperature to 650 °C with a heating rate of 10 °C min^{-1}.

Catalytic testing. Performing reactions with pressurized acetylene requires several strict safety measures (*e.g.* explosion-safe cubicle, check valves, remote control *via* magnetic valves, purging possibilities with inert gases, *etc.*). More detailed information on safety aspects when working with pressurized acetylene as well as further details about the reactor setup see the dissertation of I.-T. Trotus[41] or previously published studies by our group.[23,37,38,42,43] Catalytic testing was performed in a stainless steel plug-flow fixed bed reactor (8 mm i.d.) at 10 bar pressure and temperatures between 50 and 200 °C. An external tube oven equipped with a thermocouple ($T_{heating}$) was used to heat the reactor. The temperature inside the catalyst bed was measured at up to four different positions (T top 1, T top 2, T middle, T bottom). Hydrogen, nitrogen, ethylene, acetylene and methane gas were purchased from Air Liquide. Acetylene gas was cleaned from acetone traces *via* a bed of previously dried alumina and zeolite A extrudates and compressed to 25 bar prior to use. All other gases were used without further purification. The flow rate of gases (20 ml min^{-1} C_2H_2, 20 ml min^{-1} C_2H_4, 100 ml min^{-1} H_2 and 10 ml min^{-1} CH_4) was dosed separately *via* previously calibrated mass flow controllers to a WHSV of 84 000 cm^3 h^{-1} $g_{cat.}{}^{-1}$. Methane was added as an internal standard to the product stream after the reactor. 100 mg of catalyst, pelletized and crushed to a split size between 300 and 400 μm, was mixed with 3.0 g of silicon carbide (46 grit) as dilutant and placed onto a metal sieve inside the reactor. Quartz wool was added above to stabilize the position of the catalyst bed. All downstream tubing of the reactor was heated to 150 °C to avoid condensation of high-boiling oligomerisation products. For the compositional analysis of the feed and product gas stream an online gas chromatograph (Agilent 7890B) equipped with three sequential columns (Rxi-5Sil MS, RT-alumina BOND/Na_2SO_4, RT-Msieve 5A) from Restek and two FID and one TCD detector, respectively, was used. Flows of detected compounds (ethane, ethylene, acetylene, propane, propene, butane, 1-butene, 2-*trans*-butene, 2-*cis*-butene) were calculated *via* the peak area ratio to methane (set to a constant flow), using response factors from previous calibration. The acetylene conversion ($X_{C_2H_2}$) was determined according to eqn (1) as fraction of the molar flow of acetylene leaving ($\dot{n}_{C_2H_2,out}$) over acetylene fed into the reactor ($\dot{n}_{C_2H_2,in}$). Selectivity to ethylene, C_3 (propane, propene) and C_4 (butane, 1-butene, *trans*-2-butene, *cis*-2-butene) (S_{C_x}) were calculated *via* eqn (2) using the difference between molar flow in the feed ($\dot{n}_{C_x,in}$, when present) and product gas stream ($\dot{n}_{C_x,out}$) over the molar flow of converted acetylene taking the number of carbon atoms of the compound (a_{C_x}) into account. Carbon balance (CB) was calculated *via* eqn (3) using the molar flows of compounds in the product stream ($\dot{n}_{C_x,out}$) and in the feed ($\dot{n}_{C_x,in}$) multiplied with their number of carbon atoms (a_{C_x}). The selectivity to high-boiling hydrocarbons ($S_{C>4}$) was assessed indirectly *via* carbon missing in the carbon balance as shown in eqn (4). Overall, the catalytic tests

demonstrated good phenomenological reproducibility between different catalytic tests and material batches. Only in a few cases, unexplainable deviations were noted.

$$X_{C_2H_2} = 1 - \frac{\dot{n}_{C_2H_2,out}}{\dot{n}_{C_2H_2,in}} \quad (1)$$

$$S_{C_x} = \frac{(\dot{n}_{C_x,out} - \dot{n}_{C_x,in}) \cdot (a_{C_x}/2)}{\dot{n}_{C_2H_2,in} - \dot{n}_{C_2H_2,out}} \quad (2)$$

$$CB = \frac{\sum_{x=1}^{4} (a_{C_x} \cdot \dot{n}_{C_x,out})}{\sum_{x=1}^{4} (a_{C_x} \cdot \dot{n}_{C_x,in})} \quad (3)$$

$$S_{C_{>4}} = 100\% - \sum_{x=1}^{4} S_{C_x} \quad (4)$$

Postmortem analysis. Catalyst beds were recovered after catalytic testing, finely ground and analyzed for structural stability and the deposition of non-volatile oligomers or coke on the catalyst surface. Energy dispersive X-ray spectroscopy (EDXS) and scanning transmission electron microscopy (STEM) were performed on a Thermo Scientific Talos F200X transmission electron microscope equipped with a SuperX EDS System consisting of four silicon drift detectors. Acceleration voltage of the instrument was set to 200 kV. For sample preparation, the materials were ultrasonically suspended in acetone, 50 μL of the suspension was drop-casted on a copper lacey grid and dried under a heating lamp. For reliable comparison, fresh materials (diluted to 1 wt%) were analyzed the same way before catalysis. Thermogravimetric analysis (TGA) of the recovered finely ground catalyst bed (*ca.* 70 mg) after catalysis was performed on a Netzsch STA 449F3 instrument in the temperature range from 45 to 1000 °C (10 °C min^{-1}, 60 ml min^{-1} air). Data analysis was done *via* the Netzsch Proteus – Thermal Analysis software (version 6.1.0). The GC analysis of the red/green oil residue in the downstream piping of the reactor after reaction was performed on a GC 7890B (Agilent) equipped with an FID detector (at 350 °C) and hydrogen as eluent (1.8 bar). The oily liquid was dissolved in acetone and injected (1.0 μl, split ratio 10 : 1, injector temperature 220 °C) on a Restek Rtx-1 capillary column (60 m, 0.25 mm ID, 0.25 μm df) at 50 °C (3 °C min^{-1} ramp to 350 °C, 3 min isothermal). Time-of-flight secondary ion mass spectrometry (ToF-SIMS) was performed by the Tascon GmbH (Münster, Germany) on a TOF.SIMS 5-300 mass spectrometer (IONTOF GmbH, Münster, Germany) equipped with a Bi_3^+ ion gun (30 keV). Prior to taking ToF-SIMS spectra in positive and negative ion mode, the sample surface was cleaned from adventitious surface contaminants by sputtering with an Ar_{1500}^+ cluster ion beam ($8.38 \cdot 10^{15}$ ions per cm^2) for a few seconds. ToF-SIMS spectra were obtained with a Bi_3^+ ion beam in an incidence angle of 45°. In high mass resolution bunched mode the extraction voltage and delay time were 1000 kV and 0.045 μs, respectively. Low-energy electrons from a pulsed flood gun were used for charge neutralization. Obtained ion intensities were normalized to the total ion intensity. IONTOF SurfaceLab (version 7.3 and 7.4) software was used for measurement and data evaluation.

Results and discussion

Mechanochemical synthesis of supported Pd–Cu alloy NPs under different milling atmospheres

The supported Pd–Cu alloy NPs were synthesized under oxidative (air), inert (argon) and reductive (H_2) atmospheres using a ball milling method consisting of three steps (Fig. 1) (for technical parameters see Table S1). For the reductive atmosphere, an in-house built P6 jar (Fig. S1) was employed to address the limitations of the P7 milling jar, which cannot be used under H_2 gas. A direct comparison with oxidative and inert atmospheres is therefore somewhat limited. The milling atmosphere was carefully controlled throughout the synthesis process to ensure the required gas conditions. In the first step, Pd and Cu bulk metal powders were milled at 550 rpm for 30 minutes with three large 15 mm ZrO_2 balls to achieve the desired 5 wt% Pd–Cu bulk alloy. In the second step, γ-AlOOH powder, which has been shown to undergo dehydration during

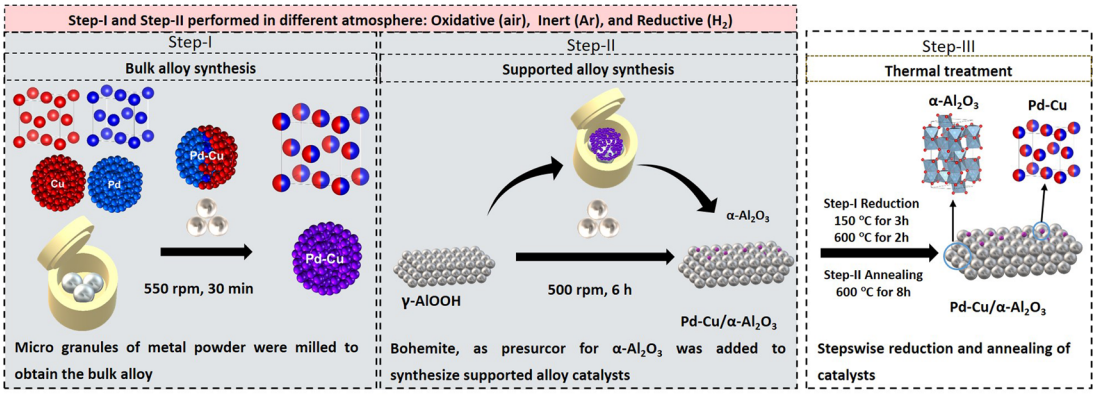

Fig. 1 Schematic illustration for the mechanochemical synthesis of supported Pd–Cu catalysts in oxidative (air), inert (Ar), and reductive (H_2) environment.

ball milling to form stable, high-surface-area α-Al_2O_3, was added to the same jar, thus achieving the α-Al_2O_3-supported Pd–Cu NPs. Although our group had previously reported a one-step ball milling synthesis of supported bimetallic catalysts,[22,24] our attempt to synthesize the Pd–Cu supported catalyst in a single step (Pd and Cu powder milled directly with boehmite) was unsuccessful. This failure is likely due to the dehydration of γ-AlOOH under release of water to form α-Al_2O_3, which may have interfered with the formation of the Pd–Cu alloy phase. It is important to note that the milling conditions in the first step were optimized to achieve effective comminution and alloying of the metal precursor, as extending the milling time or increasing the frequency did not produce significant changes. In the second step, the conditions were designed to ensure the formation of high-surface-area α-Al_2O_3, based on a previous study with slight modifications.[23] The samples were denoted as 5 wt% Pd_1Cu_1/α-Al_2O_3-oxi-bm, 5 wt% Pd_1Cu_1/α-Al_2O_3-ine-bm and 5 wt% Pd_1Cu_1/α-Al_2O_3-red-bm for oxidative, inert and reductive atmospheres, respectively.

Structural features of supported Pd–Cu catalysts synthesized in different milling atmospheres

Powder X-ray diffraction (p-XRD) (Fig. 2a and b) reveals prominent reflections for α-Al_2O_3 alongside those for traces of γ-Al_2O_3 and γ-AlOOH for oxidative and inert atmosphere samples, which is likely due to the incomplete phase transformation of the precursor as reported in previous studies.[23] In contrast, for the sample milled under reductive conditions, γ-Al_2O_3 and γ-AlOOH were the dominant phase along with minor reflections for α-Al_2O_3. Additionally, ZrO_2 reflections confirm abrasion impurities (0.4–0.8 wt%), as also confirmed by bulk scanning electron microscopy-energy dispersive X-ray spectroscopy (SEM-EDXS) analysis (Table S2). Further, p-XRD analysis proves that

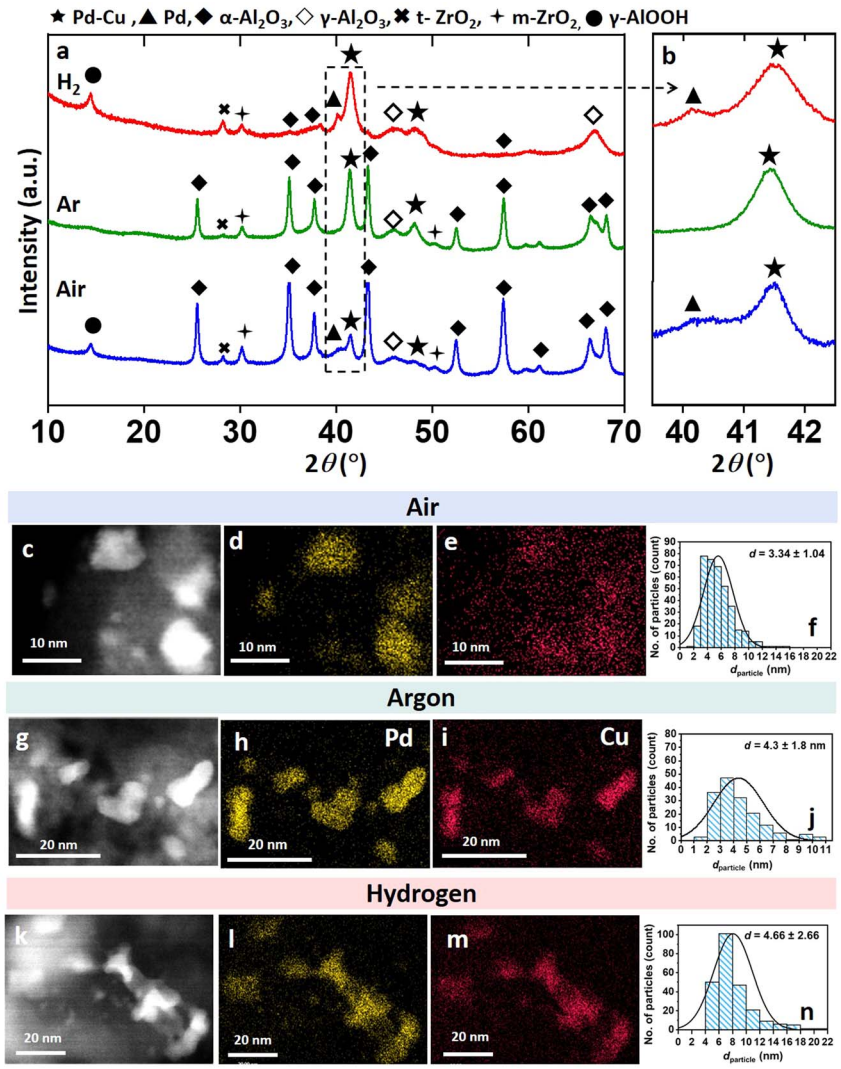

Fig. 2 p-XRD profile (a), enlarged p-XRD pattern in the 2θ range 39.5° to 42.5° (b) of 5 wt% Pd_1Cu_1/α-Al_2O_3-oxi-bm (blue), 5 wt% Pd_1Cu_1/α-Al_2O_3-ine-bm (green), 5 wt% Pd_1Cu_1/α-Al_2O_3-red-bm (red), HAAD-TEM images (c, g and k), STEM-EDXS elemental mapping for Pd (d, h and i) and Cu (e, i and m), and particle size distribution for (f, j and n) for 5 wt% Pd_1Cu_1/α-Al_2O_3-oxi-bm, 5 wt% Pd_1Cu_1/α-Al_2O_3-ine-bm, and 5 wt% Pd_1Cu_1/α-Al_2O_3-red-bm.

the ball milling of bulk metal precursors in a high-energy regime leads to the formation of the Pd–Cu alloy phase in all atmospheres. The prominent characteristic reflections for the Pd–Cu alloy (1 : 1 ratio) with $Fm\bar{3}m$ space group (*cf.* JCPDS#00-048-1551) were observed in all atmospheres. The lattice parameter, a, was calculated using the interplanar distance d_{111} from the (111) diffraction reflection, measured to be 3.77 Å in all samples, consistent with the database. Notably, distinct reflections for metallic palladium (*cf.* JCPDS #00-005-0681), were observed for samples synthesized under oxidative and reductive conditions. In contrast, the sample milled in inert atmosphere does not show reflections for metallic palladium, indicating the complete mixing of metal precursors and the formation of a uniform alloy with the targeted composition. Nevertheless, the presence of metallic Pd cannot completely be ruled out, as it may be present at a concentration below the p-XRD detection limit. Moreover, the detection of possible mixed oxide species from the p-XRD pattern was not possible due to similar angle ranges with the intensive reflections of the α-Al_2O_3 support. Although no distinct copper oxide peaks were observed in the p-XRD patterns, the possibility of the oxidation of unalloyed Cu species during sample handling cannot be fully ruled out. Due to the presence of multiple phases and overlapping reflections, it is challenging to determine the crystallite size precisely from p-XRD data with Scherrer's equation. Analogous synthesis of supported Pd_xCu_y NPs with varying Pd/Cu ratios (x : y; 1 : 0, 1 : 1, 1 : 5, 1 : 9, 0 : 1 with 5 wt% metal loading) was carried out under all atmospheres in order to check the achievable range of alloy compositions. Changing compositions of the alloys formed were confirmed by the shift of the Pd–Cu alloy reflections towards higher diffraction angles in the p-XRD patterns (Fig. S2 and Table S4) as the Cu content increases, demonstrating the linear relationship between lattice constant and Cu content, in accordance with Vegard's law.[44] The estimated Pd : Cu ratios, determined using Vegard's law from p-XRD data, were in line with the intended compositions within the experimental margin of error (Table S4). Notably, reflections for metallic Pd appeared in all samples synthesized under an oxidative and reductive atmosphere, as discussed previously, while this was not the case for any sample synthesized under an inert atmosphere. Bulk SEM-EDXS and inductively coupled plasma optical emission spectroscopy (ICP-OES) analyses further confirmed the targeted elemental compositions of Pd and Cu in the alloy NPs within the error limit (Table S2).

The high-angle annular dark-field scanning transmission electron microscopy (HAAD-STEM) (Fig. 2c, g, k, S3b, S3d, S3e and S3f) and high-resolution transmission electron microscopy (HR-TEM) images (Fig. S3a and S3c) confirm the formation of alloyed NPs for all samples. The mean particle size for the samples synthesized in an oxidative, inert, and reductive atmosphere are 3.3 ± 1.04 nm, 4.3 ± 1.8 nm, and 4.6 ± 2.66 nm, respectively (Fig. 2f, j and n). Particle sizes for the supported Pd–Cu alloy NPs synthesized in an oxidative atmosphere are overall smaller compared to the samples synthesized under an inert and reductive atmosphere. In terms of particle shape, small spherical particles alongside several elongated particles are observable in all samples (Fig. 2c, g, k and S3). These elongated particles originate most likely from the occurrence of repeated shattering and coalescence processes during high-energy ball milling.[45]

Segregation of elements is often thermodynamically favorable. Thus, high-temperature annealing promotes the segregation of low surface energy elements to the surface, while the bulk composition is dominated by the elements with high surface energy. In the case of Pd–Cu, negative enthalpy of mixing favors alloy formation over the full composition range.[44] However, the low surface energy and slightly higher oxophilicity of Cu in comparison to Pd, forces it to segregate to the surface of the alloy NPs in an oxidative atmosphere at elevated temperatures to form CuO.[46] However, in a vacuum and reducing atmosphere, (H_2 or CO) reverse segregation occurs by favoring zero-valent Pd on the surface.[7] In alloy synthesis by ball milling, mechanical impacts can overcome the initial kinetic barriers for alloy formation. During the collision of milling balls, sufficiently high impacts can cause the trapped metal nanoparticles to undergo comminution, generating new active surfaces. This is followed by coalescence leading to the alloy nanoparticle formation.[24,45,47] The newly generated active surface can easily react with the gas in the vessel. Under an oxidative atmosphere, ball milling of Pd and Cu leads to surface oxidation, causing Cu segregation due to its higher oxophilicity. In contrast, in a reductive or vacuum atmosphere reverse segregation is expected, mirroring the behaviour observed in the conventional temperature-dependent surface segregation phenomenon.[13,17,32] This is evident from the STEM-EDXS elemental mapping (Fig. 2d and e) for the samples synthesized under oxidative atmosphere showing clear concentrated spots for Pd, while Cu is dispersed all over the scanned region. Additionally, non-uniform EDXS-line scans (Fig. S3b) suggest Cu segregation on the surface with incomplete alloy formation. In contrast, the absence of oxygen in the inert atmosphere promotes Pd–Cu alloying through coalescence, which facilitates the agglomeration of particles. STEM-EDXS elemental mapping (Fig. 2h and i), where both Pd and Cu are detected in the same spots, and uniform overlapping of both elements in EDX-line scans (Fig. S3d), suggests Pd–Cu alloy formation without any surface segregation of Cu in an inert atmosphere. The same holds for the reductive atmosphere: for these samples both Pd and Cu are localized in the same spots without observable segregation or Pd enrichment on the surface (Fig. 2l, m and S3f). This behaviour deviates from the previously reported literature, underscoring the distinctive impact of ball milling under reductive conditions.[7,18]

To ensure complete alloy formation for samples ball milled under all synthesis atmospheres, the samples were further subjected to thermal treatment (see Fig. 1 and the experimental section). Fig. 3a and b show the p-XRD patterns for the samples after additional thermal treatment denoted as 5 wt% Pd_1Cu_1/α-Al_2O_3-oxi-tt, 5 wt% Pd_1Cu_1/α-Al_2O_3-ine-tt, and 5 wt% Pd_1Cu_1/α-Al_2O_3-red-tt for oxidative, inert, and reductive atmosphere, respectively. The p-XRD profiles remain, as previously discussed, dominated by reflections of the α-Al_2O_3 phase with only minor contributions from γ-Al_2O_3 for oxidative and inert atmosphere samples, and the γ-Al_2O_3 phase with a minor

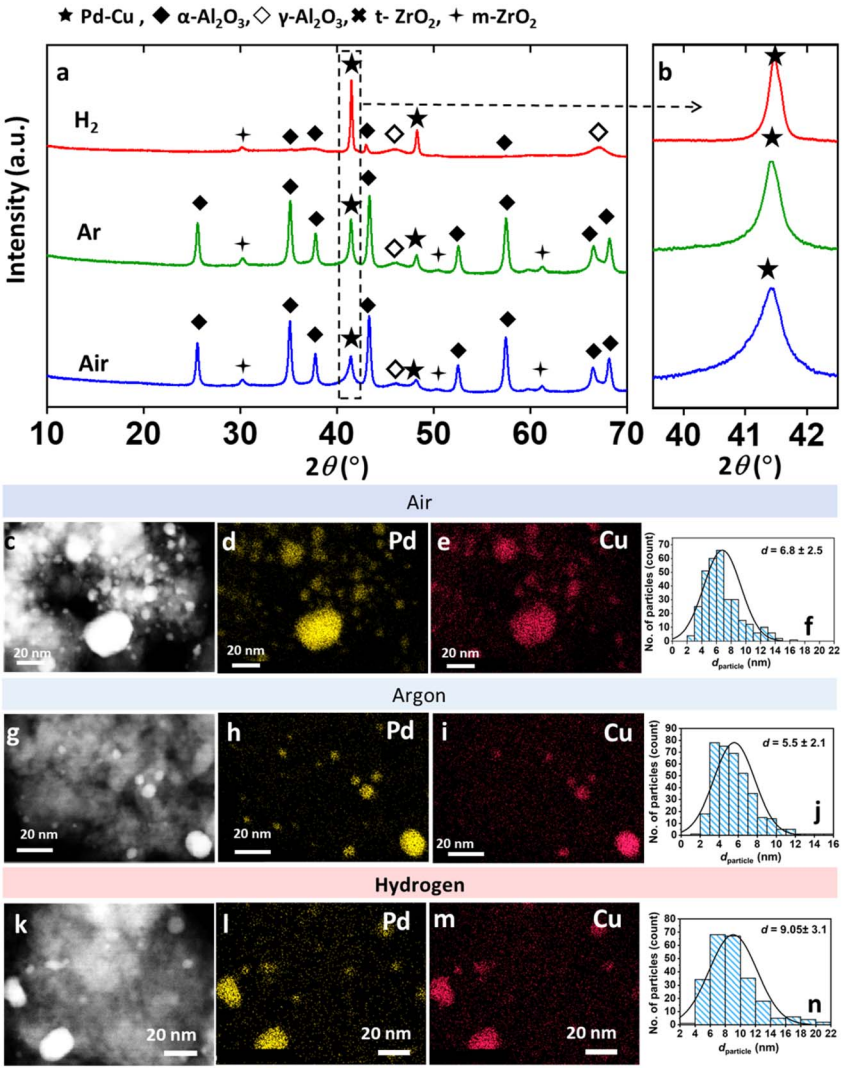

Fig. 3 p-XRD profile (a), enlarged p-XRD pattern in the 2θ range 39.5° to 42.5° (b) of 5 wt%Pd_1Cu_1/α-Al_2O_3-oxi-tt (blue), 5 wt% Pd_1Cu_1/α-Al_2O_3-ine-tt (green), and 5 wt% Pd_1Cu_1/α-Al_2O_3-red-tt (red), HAADF-STEM images (c, g and k), EDXS elemental mapping pattern for Pd (d, h and l) and Cu (e, i and m), and particle size distribution for (f, j and n) for 5 wt% Pd_1Cu_1/α-Al_2O_3-oxi-tt, 5 wt% Pd_1Cu_1/α-Al_2O_3-ine-tt, and 5 wt% Pd_1Cu_1/α-Al_2O_3-red-tt (red).

fraction of α-Al_2O_3 phase in case of the reductive atmosphere. Reflections of m-ZrO_2, attributed to abrasion form jar walls and balls, are also observed. For the sample synthesized under oxidative and reductive atmosphere, the reflections for metallic Pd have disappeared after thermal treatment, leaving only the sharp reflections of the Pd–Cu alloy. The sample prepared in inert atmosphere only contained the alloy to begin with, and thus thermal treatment did not result in substantial changes.

The positions of the reflections of the Pd–Cu alloy, and thus the lattice constant *a*, remained unchanged after the thermal treatment for all samples. Overall, p-XRD results reveal that high-energy ball milling predominantly results in alloy formation for all atmospheres. Additional thermal treatment ensures the complete alloy conversion of any residual unalloyed metal precursors remaining after ball milling.

The electron microscopy results evidence the agglomeration of alloy NPs on the support surface for all atmospheres during thermal treatment. The HAADF-STEM (Fig. 3c, g, k, S4b, d, and f) and HR-TEM images (Fig. S4a, c and e) show exclusively spherical particle morphologies with 2-fold increased average particle size for the sample synthesized under oxidative (6.8 ± 2.5 nm) and reductive (9.05 ± 3.1 nm) atmosphere. For the sample synthesized in an inert atmosphere, on the other hand, particle size increases only slightly by 1.25-fold (5.5 ± 2.1 nm) (Table S2 and Fig. 3f, j and n). STEM-EDXS mapping (Fig. 3d, e, h, i, l and m) coupled with EDXS-line scans (Fig. S4b, d and f) proves complete alloy formation in all atmospheres as both Pd and Cu were found to be localized in the same spots, uniformly overlapping with each other in accordance with p-XRD results.

Electronic properties of supported Pd–Cu catalysts synthesized in different milling atmospheres – insights from XPS and H_2-TPR analysis

X-ray photoelectron spectroscopy (XPS) analysis was performed to investigate the surface oxidation state of Pd and Cu after ball

milling in different gas atmospheres (Fig. 4 and Table S3). The Pd 3d core level spectra revealed the presence of metallic Pd(0) and surface oxides Pd(II) species for samples milled under both oxidative and inert atmosphere, whereas only a metallic Pd(0) species was detected for the sample milled under reductive atmosphere (Fig. 4a). The presence of Pd(II) species in the sample milled under argon possibly arises from the oxidation of unalloyed Pd during γ-AlOOH dehydrogenation. Due to the low Cu content in the samples, the core-level Cu 2p XPS spectra were too weak to be reliably deconvoluted. The Cu 2p core level spectra for all samples are broad and weak, even after several-fold magnification, indicating the dominance of Cu(II) species (Fig. 4b). Combined, these findings confirm the presence of metallic Pd, PdO, and CuO species, with the respective fractions depending on the milling atmosphere. Thermal treatment of ball-milled samples induces significant changes in surface species. Notably, the samples milled in air retained Pd(II) species ($3d_{5/2}$ 335.8 eV), reflecting incomplete alloy formation. In contrast, the samples milled in inert atmosphere exhibit only Pd(0) species ($3d_{5/2}$ at 334.2 eV), suggesting complete alloy formation with targeted composition (Fig. 4c). The observed *ca.* +0.9 eV binding energy shifts for the 5 wt% Pd_1Cu_1/α-Al_2O_3-oxi-tt is attributed to unalloyed Pd undergoing polarization during surface oxidation (Fig. S6).[48] Interestingly, 5 wt% Pd_1Cu_1/α-Al_2O_3-red-tt sample retains metallic Pd(0) species without any binding energy shift. Cu 2p spectra corroborated these finding, revealing both Cu(II) (935.5 eV) and Cu(0) (932.3 eV) for 5 wt% Pd_1Cu_1/α-Al_2O_3-oxi-tt, whereas only metallic Cu(0) was detected for 5 wt% Pd_1Cu_1/α-Al_2O_3-ine-tt (931.4 eV) and 5 wt% Pd_1Cu_1/α-Al_2O_3-red-tt (931.5 eV) (Fig. 4d). This suggests that oxidative milling promotes Cu segregation due to Cu's oxophilicity, limiting alloying. Thermal treatment enhances alloy formation, though residual unalloyed species persist in the sample milled under oxidative conditions. Inert atmosphere milling facilitated initial alloy formation, achieving the target composition upon thermal treatment, while reductive atmosphere milling predominantly retained metallic phases for Pd and Cu. Supporting this, H_2-temperature programmed reduction (H_2-TPR) analysis (Fig. S9) revealed distinct reduction peaks for the sample milled under oxidative conditions, weak features for the sample milled under inert conditions, and no peaks for the sample milled under reductive conditions, confirming the presence of oxide phases for oxidative milling and metallic phases in samples milled under reductive atmosphere, consistent with XPS results. Finally, no reduction peaks were observed for any thermally treated samples, supporting the conclusion of complete alloying, as inferred from XPS. In addition, XPS spectra for the O 1s and Al 2p confirm that there is no significant difference in the α-Al_2O_3 support before and after thermal treatment under any atmosphere (Fig. S7 and S8).

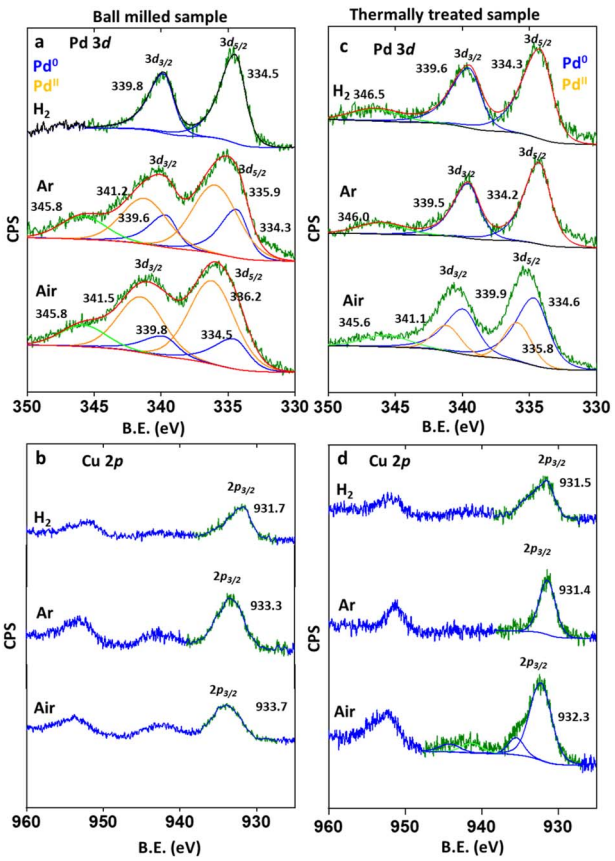

Fig. 4 XPS spectra of 5 wt% Pd_1Cu_1/α-Al_2O_3 after ball milling in oxidative (air), inert (Ar), reductive (H_2) atmospheres for Pd 3d (a) Cu 2p (b), and XPS spectra for these samples after thermal treatment for Pd 3d (c) Cu 2p (d).

Selective hydrogenation of acetylene

In order to assess the influence of structural and electronic differences on the samples' properties, we investigated their catalytic behaviour in the selective hydrogenation of equimolar acetylene/ethylene mixtures under industrially relevant pressure. These unusual gas mixtures, containing much higher acetylene concentration (≥15 vol%) than those typically found in ethylene streams from the steam cracking of naphtha (0.1 to 2 vol% C_2H_2), would be produced in a hypothetical electric plasma-assisted methane-to-ethylene conversion plant (Hüls arc process or non-thermal plasmas).[39,49–51] When integrating intermittent excess electricity from renewable energies and methane sources such as biogas or hydrogenated carbon dioxide, this pyrolysis process represents a promising sustainable pathway for ethylene production.[23,36–39] Pristine palladium catalysts typically exhibit low selectivity in the hydrogenation reaction due to similar activation barriers for desorption and further hydrogenation of ethylene. Additional (inert) metal promotors (*e.g.* Ag, Cu, Au) can spatially separate (site-isolation) and decrease the size of palladium ensembles which then provide only weaker adsorption modes for ethylene and thereby enhance selectivity. Upon sufficient alloying, those metal promotors, in addition to electronic effects (*e.g.* d-band shift), can furthermore prevent the formation of highly active but non-selective palladium hydride phases.[51–55] Non-volatile oligomeric species (green/red oil) that block active sites are a major cause of catalyst deactivation, along with coke formation, particle sintering, and alloy segregation.[52,56–58] Industrially relevant small acetylene traces (in the range of 0.1 to 2 vol%) in

ethylene coming from the steam cracker can almost completely be removed *via* selective hydrogenation with sufficiently high ethylene selectivity (>90%) and lifetime (>100 h) using this bimetallic catalyst concept.[49,51,59] Poor temperature control due to high reaction exothermicity and increased tendency of acetylene to oligomerize at higher acetylene concentrations (≥15 vol%) put particularly challenging requirements on catalysts to allow selective behaviour. Under those harsh conditions, conventionally wet-impregnated alloyed $Pd_xAg_y/\alpha\text{-}Al_2O_3$ catalysts display only moderate ethylene selectivity (≤71%) and lifetime (<10 h) at full acetylene conversion. Recently, our group demonstrated that a mechanochemical synthesis significantly increases the lifetime (>10 h) of those bimetallic catalysts while exhibiting similar selectivity.[23] Additionally, simultaneous high ethylene selectivity (>80%) and long lifetime (>20 h) under those conditions are feasible using pristine palladium catalysts coated by a thin ionic liquid layer.[37] Given the stringent requirements on catalysts to exhibit selective behaviour during selective hydrogenation at high acetylene concentration, those reaction conditions represent an ideal tool to assess the quality of alloy formation in bimetallic materials.

In order to properly investigate the materials, the 5 wt% Pd–Cu/α-Al_2O_3 samples were further diluted to 1 wt% before the thermal treatment step (Fig. S10, 11 and Table S4). The PSD for 5 wt% $Pd_1Cu_9/\alpha\text{-}Al_2O_3$ observed after dilution to 1 wt% was 3.6 ± 4.6 nm, 2.9 ± 0.86 nm, and 4.1 ± 1.2 nm for oxidative, inert, and reductive atmospheres, respectively (Fig. S12 and Table S4). Fig. 5a shows the average selectivity of 1 wt% $Pd_1Cu_9/\alpha\text{-}Al_2O_3$ synthesized under oxidative, inert and reductive conditions at different time intervals on stream in the selective hydrogenation of acetylene in equimolar ethylene mixtures at 150 °C, 10 bar pressure, and full acetylene conversion (Fig. S15–17). All samples exhibit non-selective behaviour during the first half hour on stream, fully hydrogenating not only acetylene but also the co-fed ethylene, leading to ethane selectivity between 170 and 180% and selectivities to oligomeric species ($C_{>2}$) around 20%. These non-selective properties, consistent with previous observations on pristine Pd catalysts and Pd–Ag alloys under similar reaction conditions[23,37,38] suggest the presence of larger Pd ensembles on the surface of the Pd–Cu alloys. The high reaction exothermicity leads to pronounced hotspots in the catalyst bed (*ca.* 300 °C) which are prone to favor the full hydrogenative conversion of acetylene and ethylene even in the presence of only a few larger Pd surface ensembles. With time on stream, the tendency to fully hydrogenate acetylene and co-fed ethylene is gradually decreasing for all samples, while maintaining full conversion of acetylene.

Due to the quite harsh thermal treatment (reduction with H_2 at 150 °C for 3 h followed by 600 °C for 2 h, and annealing in Ar at 600 °C for 8 h) prior to reaction, it is very unlikely that the samples undergo significant phase or structure transformations during the time on stream to alter alloy structure and decrease Pd ensemble sizes at the surface. Post catalysis TEM analysis confirms the stability of NPs for the samples from oxidative and inert atmosphere conditions as only minimal particle sintering tendencies are observed after 12–13 h (Fig. S13) or even 18 h on stream (Fig. S14). The selectivity improvement with time on

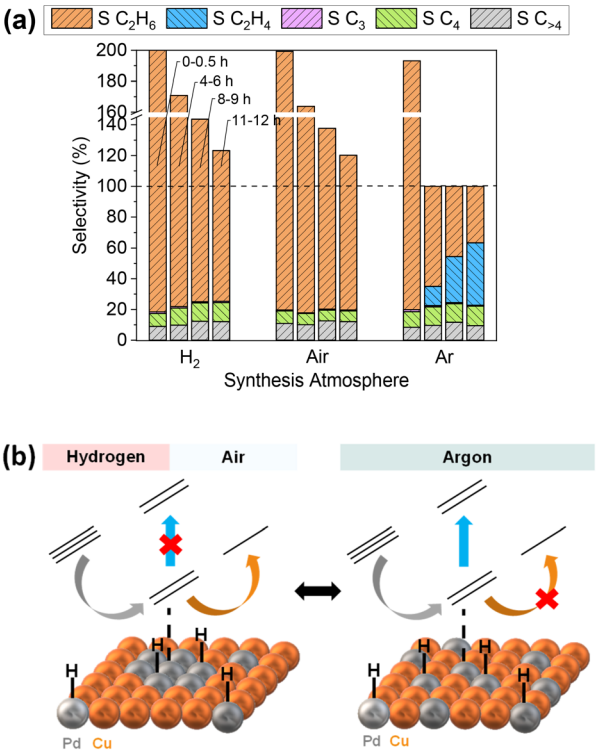

Fig. 5 (a) Average selectivity to ethane, ethylene, C_3, C_4 and $C_{>4}$ at different time intervals on stream for 1 wt% $Pd_1Cu_9/\alpha\text{-}Al_2O_3$-red-tt ($H_2$), 1 wt% $Pd_1Cu_9/\alpha\text{-}Al_2O_3$-oxi-tt (air), and 1 wt% $Pd_1Cu_9/\alpha\text{-}Al_2O_3$-ine-tt (Ar) in the selective hydrogenation of acetylene ($C_2H_2/C_2H_4/H_2$ 1 : 1:5, 10 bar, 150 °C, $X_{C_2H_2} = 100\%$, CB ≥ 0.94, WHSV 84 000 $cm^3\ h^{-1}\ g_{cat.}^{-1}$). (b) Schematic catalytic model on the effect of different Pd ensemble sizes at the surface of the three Pd–Cu alloys.

stream is hence more likely due to the blockage of non-selective larger Pd ensembles by non-volatile oligomeric species formed as by-product during reaction at such high acetylene concentration, gradually shifting reactivity towards the less active but more selective isolated Pd sites on the surface of the alloy. Even though no significant weight loss was observed for the materials after reaction in TGA experiments (Fig. S18), red/green oils could be collected from the downstream piping of the reactor after reaction. GC analysis reveals the formation of mostly even numbered oligomers, ranging from C_8 up to C_{38} (Fig. S19) in accordance with other reports in literature.[57,60] Increasing reaction temperature, thereby favoring the formation of active site blocking oligomers, significantly enhances selectivity improvement with time on stream at constant full acetylene conversion, as can be derived from Fig. 6a and S17, S20–23, which further supports this hypothesis.

The extent to which the selectivity improvement *via* non-selective site blocking is proceeding with time on stream at constant full acetylene conversion in Fig. 5a is, however, significantly different for the two catalysts. While the sample synthesized under inert atmosphere achieves selective behaviour (S C_2H_4 > 0) after 4 hours and reaches ethylene selectivity above 50% after 18 hours at constant full conversion (Fig. S17), the sample synthesized under oxidizing conditions does not

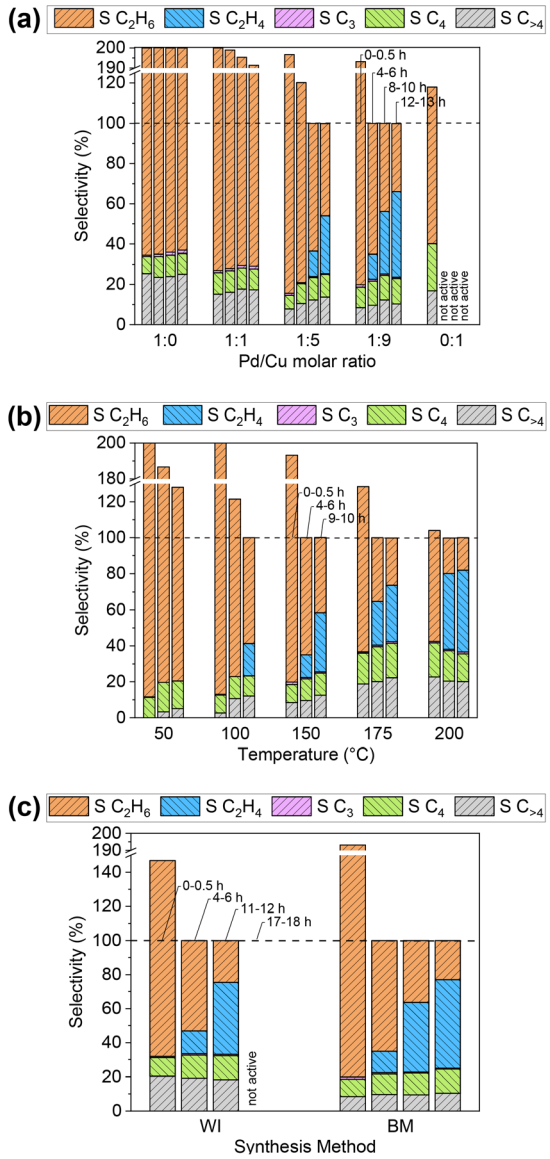

Fig. 6 Average selectivity to ethane, ethylene, C_3, C_4 and $C_{>4}$ at different time intervals on stream for (a) 1 wt% Pd_1Cu_9/α-Al_2O_3-ine-ta (Ar) at different temperatures in the selective hydrogenation of acetylene ($C_2H_2/C_2H_4/H_2$ 1 : 1 : 5, 10 bar, $X_{C_2H_2} = 100\%$, CB ≥ 0.89, WHSV 84 000 $cm^3\ h^{-1}\ g_{cat.}{}^{-1}$). (b) 1 wt% Pd_xCu_y/α-Al_2O_3-ine-tt (Ar) with different elemental compositions in the selective hydrogenation of acetylene ($C_2H_2/C_2H_4/H_2$ 1 : 1 : 5, 10 bar, 150 °C, $X_{C_2H_2} = 100\%$, CB ≥ 0.88, WHSV 84 000 $cm^3\ h^{-1}\ g_{cat.}{}^{-1}$). (c) 1 wt% Pd_1Cu_9/α-Al_2O_3-ine-tt (Ar, BM) and wet-impregnated analog (WI) in the selective hydrogenation of acetylene ($C_2H_2/C_2H_4/H_2$ 1 : 1 : 5, 10 bar, 150 °C, $X_{C_2H_2} = 100\%$, CB ≥ 0.90, WHSV 84 000 $cm^3\ h^{-1}\ g_{cat.}{}^{-1}$).

show selective behaviour even after 13 hours on stream (Fig. S16). Having approximately the same average particle size, Pd content in the alloy and a similar selectivity to oligomeric species under identical reaction conditions, this observation suggests that the sample synthesized under inert atmosphere contains fewer and/or smaller Pd ensembles in the surface of the alloy NPs. The sample synthesized under reducing atmosphere exhibits catalytic behaviour quite similar to that of the sample synthesized under oxidizing conditions (Fig. S15). Slightly larger average particle sizes (Fig. S12) and sintering phenomena observed on stream (Fig. S13) compared to the two other atmospheres, makes it, however, difficult to comparatively evaluate the catalytic behaviour across the three atmospheres. Similar non-selective catalytic behaviour as the material synthesized under oxidative atmosphere and simultaneously lower available alloy surface suggest an even higher relative share of larger non-selective Pd ensembles in the alloy, in accordance with the observed surface segregation of Pd. To prove that the observed selectivity improvement is linked to the surface structure and composition of the alloy rather than other factors (*e.g.* subsurface Pd_xC_y formation on stream[36,54,58]), different molar Pd : Cu ratios (1 : 0, 1 : 1, 1 : 5, 1 : 9, 0 : 1) with a consistent overall weight loading (1 wt%) for the synthesis procedure under inert atmosphere were tested under identical reaction conditions (Fig. S17 and 24–27). Fig. 6b shows the average selectivity for different time on stream intervals at 150 °C, 10 bar and full acetylene conversion. The results demonstrate that the extent of selectivity improvement with time on stream strongly depends on decreasing the Pd content in the alloy and with it the possible size and number of larger Pd ensembles (site isolation) in the alloy surface. The selectivity to oligomers ($C_{>2}$) is even decreasing with decreasing amount of Pd in the alloy, which is most likely linked to the fact that the (hydro-)oligomerisation of acetylene is – similar to the full hydrogenation side-reaction – favored on strongly adsorbed acetylenic species on larger Pd ensembles.[60] As the pure Pd catalyst does not contain any isolated Pd sites, it exhibits a constant non-selective behaviour (S C_2H_6 ~ 165%) over 16.5 hours on stream, while having a much higher selectivity to potentially active site blocking oligomers (S $C_{>2}$ ~ 35%) compared to the alloys (Fig. S24). The pristine Cu material is only able to fully convert acetylene in the first half hour on stream, revealing non-selective behaviour for full hydrogenation (80%) and significantly higher oligomerisation selectivity (40%) compared to the alloys (Fig. S27). It can therefore be assumed that the selective behaviour observed with time on stream for the synthesized PdCu alloys arises from isolated Pd sites surrounded by Cu atoms. Details on temperature variation on the different alloy compositions and their analogous effects on selectivity improvement with time on stream and increase in selectivity to oligomers as discussed above are provided in the electronic supplementary information (Fig. S28–39).

In order to investigate the surface composition of the alloys more precisely, the materials were analyzed *via* time-of-flight secondary ion mass spectrometry (ToF-SIMS, Fig. S40–42). Relating the semi-quantitative Pd and Cu ion intensity in the positive mode to each other reveals differences in the alloy surface composition of the samples (Fig. S42). The sample synthesized under oxidizing conditions exhibits a Cu/Pd intensity ratio of ~16, while the sample synthesized under inert conditions has a significantly higher Cu/Pd intensity ratio of ~21. This suggests, somewhat surprisingly, that the sample synthesized under inert conditions has a higher relative surface concentration of (oxophilic) Cu compared to oxidizing synthesis conditions. Higher surface concentration of Cu is of course

beneficial for the site-isolation of Pd. Although this result should be interpreted cautiously, due to the small absolute ion intensity of Pd, the only semi-quantitative nature of the method and possible error margins, this observation further supports the assumption of fewer and/or smaller Pd ensembles in the alloy surface of the sample synthesized under inert conditions. The sample synthesized, for comparison, under reducing conditions, exhibits, as expected, also a lower Cu/Pd intensity of ~15. Overall, it appears that, despite the almost identical p-XRD patterns after harsh thermal treatment with regard to the alloy formation, significant differences in the surface composition of the alloys persist, depending on the ball milling synthesis atmosphere. The atmosphere-induced segregation of Cu and Pd as CuO_x, PdO_x or Pd(–H) phases during ball milling treatment under oxidizing or reducing conditions may not only hinder full alloy formation in the mechanochemical synthesis steps, but seems to also persist at the nanoscale even after thermal treatment. This leads to more and/or larger ensembles of only Cu and Pd atoms in the surface of the alloy NPs. As discussed earlier, segregated oxide species are still detectable in the thermally activated alloy after synthesis under oxidizing conditions, supporting this interpretation.

For comparison to the mechanochemically synthesized materials, the Pd_1Cu_9 composition, supported on thermally synthesized low surface area α-Al_2O_3, was also synthesized at 1 wt% *via* a conventional wet impregnation (WI) technique (see SI, Fig. S43 and 44). Fig. 6c compares the average selectivity performance at different time intervals on stream at 150 °C, 10 bar and full acetylene conversion with the analogous material synthesized mechanochemically under inert milling atmosphere (Fig. S17 and S45). Both materials exhibit quite similar ethylene selectivity improvement with time on stream, which at first glance speaks for a comparable alloy surface composition and structure. However, considering the much higher average particle size of 26 ± 13 nm (and thus lower total alloy surface area) and the significantly higher selectivity to oligomers (~35%) of the wet-impregnated material, these results suggest that the alloy surface contains proportionally more and/or larger Pd ensembles compared to isolated Pd sites. Moreover, the wet-impregnated material deactivates after 14 hours ($X\ C_2H_2$ < 100%), whereas no loss in acetylene conversion can be observed for the mechanochemically synthesized material synthesized under inert conditions even after 18 hours on stream. The exceptional stability on-stream of the mechanochemically synthesized material is most likely due to the higher surface area of the support material and the alloy (smaller average particle size), which allows for better dispersion of the non-volatile oligomers formed as side-products.

Conclusion

This study highlights the significant impact of milling atmosphere during mechanochemical synthesis on the structural, electronic and catalytic properties of supported alloyed Pd–Cu NPs. By synthesizing Pd–Cu alloys supported on high surface area α-Al_2O_3 in a ball mill under oxidizing (air), inert (Ar), and reductive (H_2) conditions, carefully analyzing them *via* various analytical techniques before and after an additional thermal treatment and evaluating their catalytic performance in the selective hydrogenation of acetylene in equimolar mixtures with ethylene, the following conclusions can be drawn: milling in an oxidative atmosphere leads to Cu segregation to the surface due to its higher oxophilicity compared to Pd, forming CuO, PdO and Pd together with the Pd–Cu alloy phase. Milling in an inert atmosphere predominantly forms the Pd–Cu alloy phase with only trace amounts of unalloyed Pd and Cu. Unexpectedly, reductive milling atmosphere leads to the unalloyed metallic Pd along with Pd–Cu alloy phase. Thermal treatment essentially restores the alloy phase for the samples milled in oxidative and reductive atmosphere, but a small fraction of oxides still remains in sample synthesized under oxidative conditions. Investigating catalytic properties in the selective hydrogenation of acetylene in equimolar ethylene mixtures under industrially relevant pressure indicates significant differences in catalytic properties, which are attributed to differences in surface composition and structure between the different samples. The faster development of selective behaviour with time on stream together with the higher Cu/Pd surface ratio in time-of-flight secondary ion mass spectrometry (ToF-SIMS) measurements suggest better site-isolation of Pd for the sample synthesized under inert atmosphere even after harsh thermal treatment of all materials. Comparison with a conventionally wet-impregnated material suggests superior Pd site isolation properties of the supported alloy NPs synthesized under inert milling atmosphere together with an outstanding stability on stream. This study further underscores the strength of mechanochemical synthesis to achieve unique surface chemistries that might not be as easily accessible *via* conventional methods.

Author contributions

R. K., J. M. M., and F. S. designed the project, R. K. designed and optimized the mechanochemical synthesis, N. K. T. provided assistance during the synthesis. J. M. M. performed catalysis, F. S. supervised project. R. K., J. M. M. and F. S. wrote and reviewed manuscript. All authors have given approval to the final version of the manuscript.

Conflicts of interest

There are no conflicts to declare.

Data availability

The data supporting this article have been included as part of the SI. The supplementary information contains further information on the synthesis procedures and analytical and catalytic (raw) data mentioned in the main text. See DOI: **https://doi.org/10.1039/d5mr00074b**.

Acknowledgements

We thank Linfeng Li for assistance in material synthesis and sharing ball-milling equipment. We are grateful to Silvia Palm

and Norbert Pfänder (MPI for Chemical Energy Conversion) for their support in the electron microscopy analysis of the samples, as well as to Jan Ternieden, Sebastian Leiting and Claudia Weidenthaler for XRD and XPS analysis. We thank Florian Baum and Harun Tüysüz for ICP-OES analysis, Phil Hesse for GC analysis and Kathrin Röhrich, Elke Tallarek and Karsten Lamann from Tascon GmbH (Münster, Germany) for ToF-SIMS measurements. We are thankful to Sabrina Brunner and Henning Buchholz for their assistance in the lab. We are grateful to the fine mechanic workshop (led by Dirk Ullner), technical laboratories (led by Nils Theyssen) and the chromatography and electrophoresis service departments (led by Philipp Schulze) for the support in building modified jars, maintaining the milling instruments and the catalytic setup and its sophisticated safety structure. J. M. M. is thankful for a Kekulé scholarship by Fonds der Chemischen Industrie (FCI).

References

1 P. Munnik, P. E. de Jongh and K. P. de Jong, *Chem. Rev.*, 2015, **115**, 6687–6718.
2 Z. Luo, G. Zhao, H. Pan and W. Sun, *Adv. Energy Mater.*, 2022, **12**, 2201395.
3 M. Sankar, N. Dimitratos, P. J. Miedziak, P. P. Wells, C. J. Kiely and G. J. Hutchings, *Chem. Soc. Rev.*, 2012, **41**, 8099–8139.
4 W. Yu, M. D. Porosoff and J. G. Chen, *Chem. Rev.*, 2012, **112**, 5780–5817.
5 L. C. A. van den Oetelaar, O. W. Nooij, S. Oerlemans, A. W. D. van der Gon, H. H. Brongersma, L. Lefferts, A. G. Roosenbrand and J. A. R. van Veen, *J. Phys. Chem. B*, 1998, **102**, 3445–3455.
6 F. F. Tao, S. Zhang, L. Nguyen and X. Zhang, *Chem. Soc. Rev.*, 2012, **41**, 7980–7993.
7 P. Ekborg-Tanner and P. Erhart, *J. Phys. Chem. C*, 2021, **125**, 17248–17260.
8 L. Deng, W. Y. Hu, H. Q. Deng and S. F. Xiao, *J. Phys. Chem. C*, 2010, **114**, 11026–11032.
9 F. Baletto, C. Mottet and R. Ferrando, *Phys. Rev. Lett.*, 2003, **90**, 135504.
10 F. Calvo, *Phys. Chem. Chem. Phys.*, 2015, **17**, 27922–27939.
11 X. Xiang, J. L. Nie, K. Sun, L. Zhang, W. Liu, J. Schwank, S. F. Wang, M. Zhong, F. Gao and X. T. Zu, *Nanoscale*, 2014, **6**, 12898–12904.
12 L. Peng, E. Ringe, R. P. Van Duyne and L. D. Marks, *Phys. Chem. Chem. Phys.*, 2015, **17**, 27940–27951.
13 Y. Jiang, A. M. H. Lim, H. Yan, H. C. Zeng and U. Mirsaidov, *Adv. Sci.*, 2023, **10**, e2302663.
14 J. Suntivich, Z. C. Xu, C. E. Carlton, J. Kim, B. H. Han, S. W. Lee, N. Bonnet, N. Marzari, L. F. Allard, H. A. Gasteiger, K. Hamad-Schifferli and Y. Shao-Horn, *J. Am. Chem. Soc.*, 2013, **135**, 7985–7991.
15 J. J. Huang, Y. Y. Song, D. D. Ma, Y. P. Zheng, M. S. Chen and H. L. Wan, *Chin. J. Catal.*, 2017, **38**, 1229–1236.
16 M. Kalyva, M. F. Sunding, A. E. Gunnæs, S. Diplas and E. A. Redekop, *Appl. Surf. Sci.*, 2020, **532**, 147369.
17 L. Pasquale, S. Najafishirtari, R. Brescia, A. Scarpellini, C. Demirci, M. Colombo and L. Manna, *Chem. Mater.*, 2021, **33**, 8635–8648.
18 K. Sun, J. Liu, N. K. Nag and N. D. Browning, *J. Phys. Chem. B*, 2002, **106**, 12239–12246.
19 Ö. Agbaba, *MechSyn*, **https://www.kofo.mpg.de/989755/MechSyn**, accessed 20.02.2025.
20 S. Triller, A. Amrute and F. Schüth, *Ind. Eng. Chem. Res.*, 2025, **64**, 1577–1586.
21 H. Schreyer, R. Eckert, S. Immohr, J. de Bellis, M. Felderhoff and F. Schuth, *Angew Chem. Int. Ed. Engl.*, 2019, **58**, 11262–11265.
22 J. De Bellis, M. Felderhoff and F. Schüth, *Chem. Mater.*, 2021, **33**, 2037–2045.
23 K. S. Kley, J. De Bellis and F. Schüth, *Catal. Sci. Technol.*, 2023, **13**, 119–131.
24 J. De Bellis, H. Petersen, J. Ternieden, N. Pfander, C. Weidenthaler and F. Schuth, *Angew Chem. Int. Ed. Engl.*, 2022, **61**, e202208016.
25 T. Tsuzuki, *Commun. Chem.*, 2021, **4**, 143.
26 N. J. Divins, A. Braga, X. Vendrell, I. Serrano, X. Garcia, L. Soler, I. Lucentini, M. Danielis, A. Mussio, S. Colussi, I. J. Villar-Garcia, C. Escudero, A. Trovarelli and J. Llorca, *Nat. Commun.*, 2022, **13**, 5080.
27 M. Danielis, S. Colussi, C. de Leitenburg, L. Soler, J. Llorca and A. Trovarelli, *Angew Chem. Int. Ed. Engl.*, 2018, **57**, 10212–10216.
28 M. Danielis, L. E. Betancourt, I. Orozco, N. J. Divins, J. Llorca, J. A. Rodríguez, S. D. Senanayake, S. Colussi and A. Trovarelli, *Appl. Catal., B*, 2021, **282**, 119567.
29 A. Mussio, M. Danielis, N. J. Divins, J. Llorca, S. Colussi and A. Trovarelli, *ACS Appl. Mater. Interfaces*, 2021, **13**, 31614–31623.
30 E. Marín, X. Vendrell and J. Llorca, *ACS Appl. Nano Mater.*, 2025, **8**, 12151–12163.
31 S. Steinhauer, J. Zhao, V. Singh, T. Pavloudis, J. Kioseoglou, K. Nordlund, F. Djurabekova, P. Grammatikopoulos and M. Sowwan, *Chem. Mater.*, 2017, **29**, 6153–6160.
32 M. Zhao, J. C. Brouwer, W. G. Sloof and A. J. Böttger, *Int. J. Hydrogen Energy*, 2020, **45**, 21567–21572.
33 R. Khobragade, P. Dahake, N. Labhsetwar and G. Saravanan, *New J. Chem.*, 2021, **45**, 4246–4252.
34 A. P. Amrute, Z. Lodziana, H. Schreyer, C. Weidenthaler and F. Schuth, *Science*, 2019, **366**, 485–489.
35 P. A. ZielińAski, R. Schulz, S. Kaliaguine and A. Van Neste, *J. Mater. Res.*, 2011, **8**, 2985–2992.
36 Z. H. Li, E. Öztuna, K. Skorupska, O. V. Vinogradova, A. Jamshaid, A. Steigert, C. Rohner, M. Dimitrakopoulou, M. J. Prieto, C. Kunkel, M. Stredansky, P. Kube, M. Götte, A. M. Dudzinski, F. Girgsdies, S. Wrabetz, W. Frandsen, R. Blume, P. Zeller, M. Muske, D. Delgado, S. Jiang, F. P. Schmidt, T. Köhler, M. Arztmann, A. Efimenko, J. Frisch, T. M. Kokumai, R. Garcia-Diez, M. Baer, A. Hammud, J. Kroehnert, A. Trunschke, C. Scheurer, T. Schmidt, T. Lunkenbein, D. Amkreutz, H. Kuhlenbeck, V. J. Bukas, A. Knop-Gericke, R. Schlatmann, K. Reuter,

B. R. Cuenya and R. Schlögl, *Nat. Commun.*, 2024, **15**(1), 10660.
37 J. M. Mauss and F. Schüth, *Chemsuschem*, 2025, **18**(2), e202401593.
38 J. O. Williams, E. Kitching, R. S. Patel, J. M. Mauss, K. S. Kley, R. Khobragade, J. de Bellis, D. J. Morgan, T. Slater, F. Schueth, S. H. Taylor, N. F. Dummer, M. Bender and G. J. Hutchings, *Chemcatchem*, 2025, **17**, e202401794.
39 E. Delikonstantis, M. Scapinello and G. D. Stefanidis, *Fuel Process. Technol.*, 2018, **176**, 33–42.
40 L. F. Li, M. Leutzsch, P. Hesse, C. H. Wang, B. L. Wang and F. Schüth, *Angew. Chem., Int. Ed.*, 2025, **64**, e202413132.
41 I.-T. Trotus, PhD thesis, Ruhr-Universität Bochum, 2016.
42 I. T. Trotus, T. Zimmermann, N. Duyckaerts, J. Geboers and F. Schuth, *Chem. Commun.*, 2015, **51**, 7124–7127.
43 Ö. T. Agbaba, I. Teodor, W. Schmidt and F. Schüth, *Ind. Eng. Chem. Res.*, 2023, **62**, 1819–1825.
44 P. Subramanian and D. Laughlin, *J. Phase Equilib.*, 1991, **12**, 231–243.
45 J. S. Benjamin, *Sci. Am.*, 1976, **234**, 40–49.
46 K. A. Moltved and K. P. Kepp, *J. Phys. Chem. C*, 2019, **123**, 18432–18444.
47 O. V. Lapshin, E. V. Boldyreva and V. V. Boldyrev, *Russ. J. Inorg. Chem.*, 2021, **66**, 433–453.
48 D. Bagchi, M. Riyaz, N. Dutta, G. Chawla, S. R. Churipard, A. K. Singh and S. C. Peter, *Adv. Energy Mater.*, 2024, **14**, 2402237.
49 T. D. Shittu and O. B. Ayodele, *Front. Chem. Sci. Eng.*, 2022, **16**, 1031–1059.
50 I. T. Trotus, T. Zimmermann and F. Schuth, *Chem. Rev.*, 2014, **114**, 1761–1782.
51 X. X. Cao, B. L. Jang, J. X. Hu, L. Wang and S. Q. Zhang, *Molecules*, 2023, 28.
52 M. R. Ball, K. R. Rivera-Dones, E. B. Gilcher, S. F. Ausman, C. W. Hullfish, E. A. Lebron and J. A. Dumesic, *ACS Catal.*, 2020, **10**, 8567–8581.
53 F. Studt, F. Abild-Pedersen, T. Bligaard, R. Z. Sorensen, C. H. Christensen and J. K. Norskov, *Science*, 2008, **320**, 1320–1322.
54 F. Studt, F. Abild-Pedersen, T. Bligaard, R. Z. Sorensen, C. H. Christensen and J. K. Norskov, *Angew. Chem., Int. Ed.*, 2008, **47**, 9299–9302.
55 L. L. Zhang, M. X. Zhou, A. Q. Wang and T. Zhang, *Chem. Rev.*, 2020, **120**, 683–733.
56 Q. S. Luo, H. Wang, L. Wang and F. S. Xiao, *ACS Mater. Au*, 2022, **2**, 313–320.
57 H. X. Su, Y. Jiao, J. G. Shi, Z. W. Yuan, D. Zhang, X. P. Wang, J. Ren, D. Liu, J. Z. Gui, H. Y. Gao and X. L. Xu, *Petrol. Sci.*, 2024, **21**, 1405–1414.
58 M. Kuhn, M. Lucas and P. Claus, *Ind. Eng. Chem. Res.*, 2015, **54**, 6683–6691.
59 L. Chen, X. T. Li, S. C. Ma, Y. F. Hu, C. Shang and Z. P. Liu, *ACS Catal.*, 2022, **12**, 14872–14881.
60 E. Vignola, S. N. Steinmann, A. Al Farra, B. D. Vandegehuchte, D. Curulla and P. Sautet, *ACS Catal.*, 2018, **8**, 1662–1671.